Rock and Soil Mechanics 2026 47(4): 1129−1146 ISSN 1000−7598
https: //doi.org/10.26599/RSM.2025.94300235 journal homepage: rocksoilmech.whrsm.ac.cn

Evaluation of the feasibility of using 3D LCD-Printed samples as rock analogs in geomechanical studies

Evgenii Kozhevnikov[1], Mikhail Turbakov[1], Zakhar Ivanov[2], Evgenii Riabokon[1], Andrei Golosov[3], Mikhail Guzev[1], Evgenii Gladkikh[1], Daniil Katunin[2], Pavel Kamenev[4]1. Department of Oil and Gas Technologies, Perm National Research Polytechnic University, Perm 614990, Russia;

2. Laboratory of Natural Gas Hydrates, Perm National Research Polytechnic University, Perm 614990, Russia;

3. Research and Educational Centre for Geomechanics and Geodynamics of Highly Compressed Rocks and Rock Masses, Far Eastern Federal University, Vladivostok 690041, Russia;

4. Laboratory of Geochemistry and Regional Geology, Institute of Marine Geology and Geophysics of the Far Eastern Branch of the Russian Academy of Sciences, Yuzhno-Sakhalinsk, Russia;

Abstract: 3D printing has emerged as a valuable tool for studying the mechanical behavior of rock replicas under various stress−strain states. This technique enables the creation of an unlimited number of replicas with predetermined properties and a homogeneous structure. Among various 3D printing methods, liquid crystal display (LCD)-based printing offers a cost-effective and high-quality approach for rapid prototyping of rock samples. This study investigates the feasibility of using 3D LCD printing to create rock analogs for geomechanical investigations. We evaluate the microstructure of LCD-printed samples and its influence on their elastic and mechanical properties. To assess these properties, we subjected cylindrical samples to elastic wave propagation and uniaxial compression tests. Our results demonstrate that LCD-printed samples exhibit high homogeneity of elastic properties. The velocities of elastic wave propagation across and along the layers are essentially identical, differing only by the error value. Moreover, Young's moduli obtained under uniaxial loading are in good agreement with non-destructive test results, indicating a high degree of homogeneity in elastic properties up to 20 MPa. These findings suggest that 3D LCD-printed rock analogs are well-suited for investigating processes in rocks under purely elastic loading. Additionally, the technology's versatility allows for the creation of rock replicas with various features, providing researchers with the ability to study the mechanical behavior of rocks with specific characteristics. We demonstrate the potential of 3D LCD-printed rock analogs through a case study investigating the impact of cyclic deformations on the conductivity of thin capillaries in a porous medium. Our results provide a strong foundation for utilizing 3D LCD printing to advance our understanding of geomechanical processes in rocks.

Keywords: 3D printing; uniaxial compression; anisotropy; Young's modulus; Poisson's ratio; permeability

1 Introduction

Rapid prototyping finds widespread application across diverse fields, including in the creation of rock replicas[1]. The creation of rock replicas is increasingly employed in the mining and oil industries for the study of rock properties, including their permeability based on internal structure[2] and their response to mechanical loading[3]. Using 3D printing it is possible to make unlimited number of copies and enabling the implementation of a wide range of destructive research methods.

Today, there are various technologies for creating 3D models of rocks. The choice of printing technology depends on the intended purpose and the material required. Samples can be manufactured using fused deposition modeling (FDM)[4] or fused filament fabrication (FFF)[5] technologies, which are based on layer-by-layer fusion of material, mainly plastic. Plastic samples produced using these technologies are rarely applicable as rock-like analogues, due to the low printing resolution and the structure and properties of the material, which are very far from natural rocks. To create the closest analogues of rocks, gypsum or quartz sand is used as the source material, which is bonded using a special hardener–furanic acid, cyanoacrylate glue, furfuryl alcohol and phenolic resins, or a mixture of cement, silica and water. The production of rocks using mineral components can bring the mechanical and strength properties of replicas closer to real rocks, but these methods are characterized by low printing resolution and are not able to reproduce the internal structure of a unique sample based on computed tomography (CT)[6].

Stereolithography (SLA) technology currently boasts the highest print quality and finds utility beyond practical applications, extending to research purposes. This is because SLA allows for the precise replication of micro-heterogeneities present in original objects. The SLA method can be classified, depending on the photopolymer resin curing approach, into laser-based (e.g., laser SLA) [7-8], digital light processing (DLP)[9] and liquid crystal display-based (LCD)[10]. These methods are based on layer-by-layer photopolymer resin curing. The resolution of SLA printing is the highest of all rapid prototyping methods. SLA printing is widely used in geosciences, especially in the production of porous and fractured rock replicas[11-12]. However, the production of porous media similar to natural rocks is complicated by the insufficient resolution of digital models and printing, which is often

Received: 23 April 2025 Accepted: 14 October 2025
This work was supported by the Russian Science Foundation (23-19-00699).
First author: Evgenii Kozhevnikov, male, born in 1991, PhD, Associate Professor, mainly engaged in research on petroleum engineering.
E-mail: kozhevnikov_evg@mail.ru

larger than the size of pores and heterogeneities. Also, after printing, it is very difficult to clean the porous medium from resin residues, which leads to distortion of the pore space and difficulties with flooding. To avoid these difficulties, some studies suggest replacing porous media with solid models with a conductive channel, such as a spiral shape[13] or in the form of cracks[14]. With a single channel, it is easier to achieve its high quality and purity of experimental conditions.

Thus, among all rapid prototyping methods, SLA printing is the most promising for the production of rock samples for geoscience research, as it allows achieving a high degree of replication. However, the deformation behavior of 3D SLA printed samples under loading, especially under compression, remains poorly understood. There are also no assessments of the suitability of 3D SLA printed samples for cyclic compression, despite the fact that many works have been devoted to the study of the mechanical properties of 3D SLA printing.

Mechanical properties of 3D SLA printed samples are most influenced by the printing and curing conditions. However, all else being equal, a defining characteristic of stereolithography printing is the layer-by-layer heterogeneity of the resulting parts. The layered structure leads to variations in the strength characteristics depending on the angle and orientation of the layers. This variability arises from the heterogeneity inherent in each layer and the presence of inter-layer contacts.

Numerous studies have investigated the impact of SLA printing angle on the mechanical properties of fabricated parts. Rigorous review showed that the results of experimental studies of the influence of angle and orientation of layers can be opposite. Independent groups of authors[15–19] have experimentally investigated the effect of the printing angle on the strength of 3D printed parts under compression and tension. The authors come to the general conclusion that samples in which the tensile force under pure tension is parallel to the layers have the highest Young's modulus and strength. Specimens with inclined layers have the highest compressive properties[17]. Li and Teng[15] attributed this phenomenon to weaker bonding between the layers, suggesting that the angle of the layers influences the cohesive strength of the material. Also authors point out that the strength is affected by the presence of defects in the parts, which are formed due to printing features – uneven edges, air bubbles, foreign inclusions.

While the above-mentioned works state that the samples have greater strength when stretched along the printing layers, other studies[20–24] have experimentally established that the strength of samples with layers oriented parallel to the tensile load is lower than that of samples with a perpendicular direction. Puebla et al[20] indicate that the reason for the different strength of the samples is the different direction of laser movement during curing. Cosmi and Maso[23] experimentally established that the Young's modulus is the highest in SLA printed samples with a tensile load directed perpendicular to the layers, but the strength and deformation are higher in samples with an angular direction. Pandzic[24] investigated the effect of the thickness and orientation of SLA samples layers relative to the load on the tensile strength and established that the smaller the layer thickness, the higher the strength and elastic characteristics. In samples with layers perpendicular to the load, the Young's modulus is slightly higher, but the strength is noticeably lower at any layer thickness. Reducing the layer thickness in the direction perpendicular to the load increases the brittleness of the material, which is reflected in an increase in rigidity and a decrease in strength.

Despite extensive research on the influence of layer orientation on the strength properties of 3D printed parts, a significant gap exists in the literature. Most studies focus primarily on tensile strength, with limited investigation into compressive strength. Furthermore, experimental results regarding the impact of layer orientation on strength are inconsistent. This lack of consistency hinders a definitive understanding of the underlying failure mechanism and the factors contributing to strength variations with respect to printing layer direction. In this regard, to assess the applicability of 3D LCD replicas of rocks for research in geosciences, an additional assessment of the mechanical characteristics of the samples is necessary depending on the printing conditions, post-processing and layer orientation. In this paper, the feasibility of 3D LCD replicas of rocks for research in geosciences is assessed based on the analysis of the microstructure of the printed replicas and non-destructive and destructive tests. Comparative results of uniaxial compression strength (UCS) and cyclic flooding of a real rocks and a 3D LCD printed replica are also presented.

2 Methodology

2.1 Sample printing and post-processing

The samples were manufactured in several stages

(1) Digital modelling in Computer-Aided Design (CAD) software;

(2) Printing;

(3) Washing;

(4) Samples turning on lathe for shapes in accordance with the ASTM D7012-23 standard[25];

(5) Curing and P/S wave testing.

The digital model was sized according to ASTM D7012-23[25] with a length to diameter ratio of 2:1 and was 70 mm long and 35 mm in diameter. The digital model was exported to stl format for subsequent prepress. In the slicer software, the samples were placed on the work table with different layer angles (Fig.1), 3 samples for each printing angle. Angles 90º, 60º, 30º and 0º are the angles between the layer plane and the sample axis. To maintain geometry, the samples were printed with supports. All samples are oriented along the *Y* axis of the printer.

Samples were printed on an Anycubic Photon Mono

X (Anycubic) printer by the LCD method (see Fig.2(a)), which is the cheapest and most accessible type of SLA printing, and has a fairly high print quality. The printing parameters are given in Table 1. The exposure time was 2 s and was determined during preliminary tests for ensuring high printing quality and speed. The layer thickness was set by default and is 50 μm for the Anycubic Photon Mono X printer. Commercial resin Anycubic Basic Resin Black™ was used for printing. The black resin was chosen to minimize the effect of unwanted light scattering on print quality.

After printing, the samples were washed in an ultrasonic bath with isopropyl alcohol. Cylindrical samples with an approximate diameter of 35 mm and a length of 70 mm were obtained (see Fig.2(b)). The specimens printed with parallel and inclined layers have an irregular cylindrical shape due to the layer sagging during printing (see Fig.2(b)). The ends of these cylinders have non-parallel surfaces, protrusions, irregularities and pimples. There were defects on the ends associated with underprinting.

Table 1 Sample printing parameters

Platform lifting distance /mm	Platform lifting speed /(mm • s^{-1})	Platform retract speed /(mm • s^{-1})	Layer thickness /μm	UV power /%	Normal exposure time/s
5	3	3	50	100	2

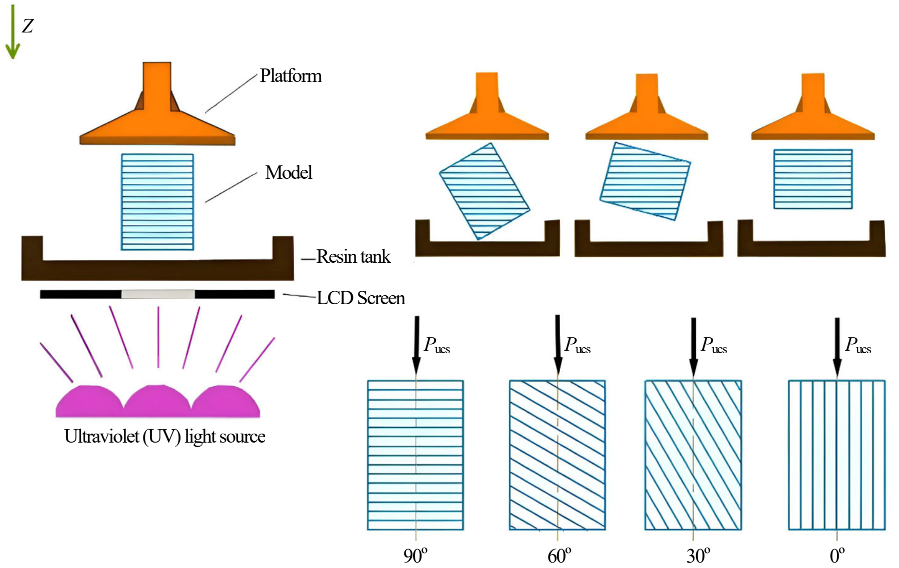

Note: The angle value is the angle between the layers and the load vector (P_{ucs}) under uniaxial compression.

Fig.1 Schematic representation of printing samples with different layer printing angles

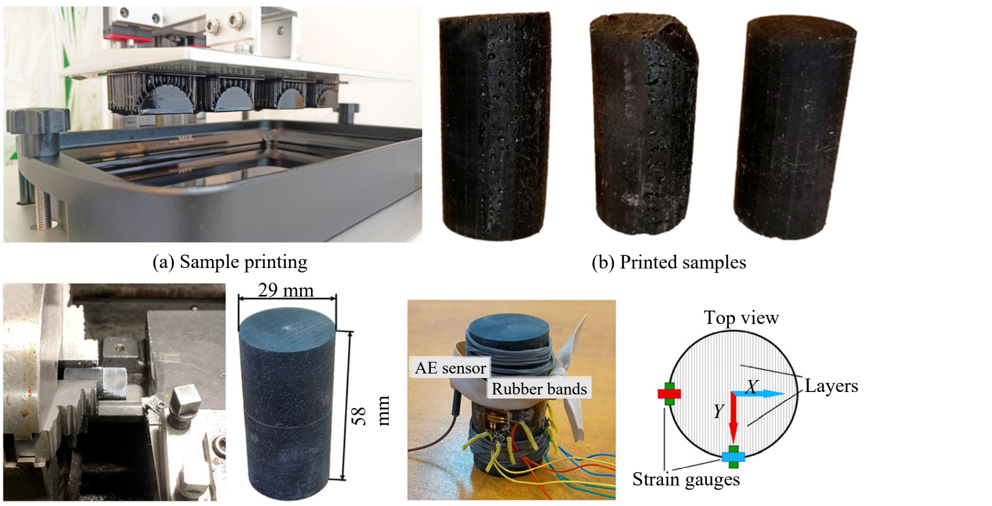

(a) Sample printing (b) Printed samples

(c) Samples turning (d) Finished sample with acoustic emission (AE) sensor and strain gauges

Fig.2 Samples manufacturing steps

The specimens were initially designed of slightly larger size for post-processing with a lathe (see Fig.2(c)). The specimens ready for testing have a regular cylindrical shape with parallel edges with a diameter of 29 mm and a length of 58 mm, which meets the ASTM D7012-23 standard[25]. The finished specimens were cured in a UV chamber. Before testing, the specimens were stored in a dark place to minimize exposure to natural light. Storage temperature and humidity correspond to normal room conditions. All specimens were kept in the same conditions, and storage conditions should not affect the results[22, 24, 26].

2.2 P-S waves velocities

Non-destructive testing of mechanical parameters of rocks involves measuring the velocity of ultrasonic elastic pressure and shear waves. The wave velocity was measured on a device using a point source and receiver tightly pressed to the printed sample from opposite sides. The operating frequency of ultrasound is 140−500 kHz, which corresponds to wavelengths from 3 to 10 mm, which is much greater than the thickness of the layers from which the samples are made. The velocity of elastic waves was measured every minute of curing in a UV chamber (see Fig. 3(a)). Wave velocities were measured in the axial and radial directions (see Fig. 3(b), 3(c)) parallel and perpendicular to the printed layers.

(a) Sample in UV curing chamber (b) Schematic diagram of elastic wave velocity measurement in axial direction (c) Schematic diagram of elastic wave velocity measurement in radial direction

Fig.3 Non-destructive testing of rocks

2.3 Rocks

Since the printed samples were considered to be homogeneous, rocks with a homogeneous fine-crystalline structure were selected for comparison − silicites, which are microgranular quartz (groups 1 and 2), silicified dolomites (group 3) and opoka (group 4). To evaluate a wide range of strength, as well as anisotropy, samples of different strengths were selected and made perpendicular (groups 1 and 3) and parallel to bedding (groups 2 and 4). Cylindrical samples were made in sizes 30 mm×60 mm for mechanical tests (see Fig. 4) and 30 mm×30 mm for filtration studies (see Fig. 20).

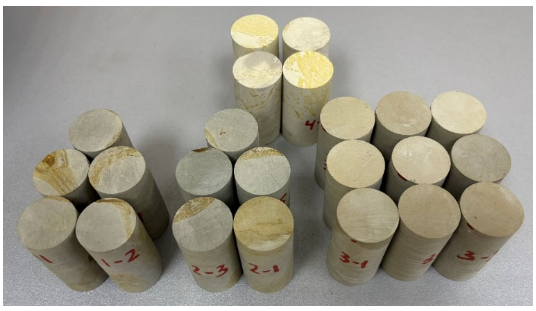

Note: 1and 2 are silicites, 3 is silicified dolomites, and 4 is opoka.

Fig.4 Cylindrical samples of silicites, silicified dolomites and opoka for uniaxial compression

2.4 Uniaxial compression test

Uniaxial compression was performed using a rock mechanics test system 816. Strain gauges glued to the side surface of the specimens (see Fig. 2(d)) and a data acquisition system of the loading rig were used to measure transverse and longitudinal strains. Two pairs of strain gauges were positioned relative to the printer axes as shown in Fig. 2(d). An acoustic emission(AE) sensor was attached to the middle of the side surface of the specimens using a rubber belt.

During loading, data from the load cell, strain gauges, and AE signal acquisition system were recorded on a computer. Uniaxial compression was performed until the specimen failed. The loading rate for all specimens was 0.1 MPa/s in accordance with ASTM D7012-23[25]. Poisson's ratio was calculated based on strain gauge data and only for the quasi-elastic deformation zone. The total axial strain is taken from the load cell's displacement data.

3 Results

3.1 Assessment with non-destructive research methods

The non-destructive technique involves measuring the velocity of elastic pressure and shear waves. The velocity of the waves shows changes in mechanical properties over time, and can also estimate the anisotropy of materials and rocks. The study of the mechanical parameters of photopolymer resins using non-destructive methods is vital, since the material changes its properties during post-processing during ultraviolet irradiation and storage, and also has a layered structure that affects the mechanical parameters [24, 27].

3.1.1 Changes in mechanical properties during processing

The sufficiency of the post-curing exposure time to ultraviolet light was judged by the unchanged elastic wave velocity. Wave velocities from the duration of UV curing are presented in the graphs (see Fig. 5). After 1 minute of exposure, the velocity of elastic waves increases sharply compared to the untreated sample, and then changes slightly, which indicates that 1 minute of exposure is sufficient for external strengthening of the sample. 4 minutes of exposure to ultraviolet light is enough to achieve complete polymerization of the sample material, after which further exposure does not change the mechanical properties. With further exposure, ultraviolet light does not penetrate into the sample, and longer exposure to ultraviolet light is not necessary, this is confirmed by the constant velocity of elastic waves after 8 minutes of exposure to UV. It was also found that storage time does not affect the internal polymerization of the sample material stored in room conditions in a dark place. The velocity of pressure and shear waves remained at the same level after 14 days of storage (see Fig. 5).

3.1.2 Anisotropy

The anisotropy of the samples was estimated by the P-S wave velocities along the axis and across the samples (parallel (||) and perpendicular (⊥) to the printed layers) (see Figs. 3(b), 3(c)). Parallel and transverse directions of measurements are sufficient, since in these two directions the layered materials show the greatest difference in mechanical properties[28]. The results of the studies showed that the wave velocities across and along the layers are the same and differ only by the error value. The same value of Young's moduli and shear (see Fig.5) indicates a high degree of isotropy of 3D LCD printed samples, when measuring elastic properties using a non-destructive method.

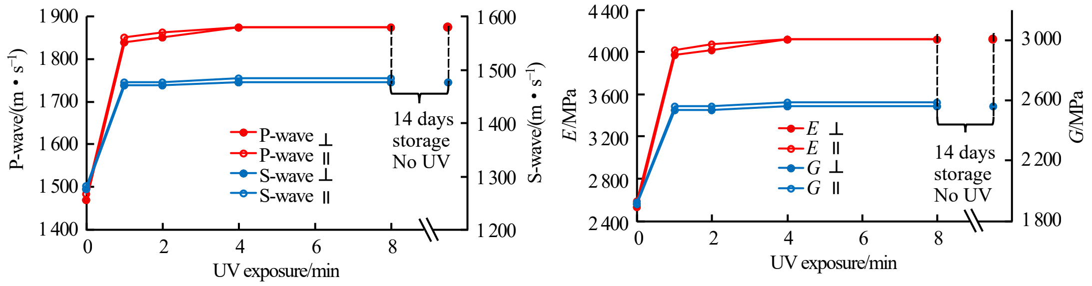

(a) Elastic wave velocities (b) Young's and shear moduli

Fig.5 Changes in elastic wave velocities and Young's and shear moduli depending on the duration of post-curing and storage time

Anisotropy of rock properties is related to the formation conditions and is usually a consequence of the bedding angle of the layers or the direction of stress in the bedding conditions. Using a non-destructive test, the values of Young's modulus were obtained for rock samples (see Fig. 6). According to the non-destructive method, the most elastic rocks are silicified dolomites, and the less elastic ones are opoka.

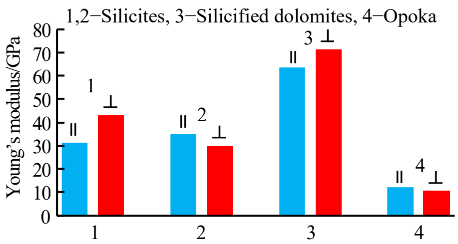

Fig.6 Average values of Young's modulus for rocks

It was found that in the samples (groups 1 and 3) drilled across the bedding, the elastic wave velocity and the calculated modulus along the sample axis are lower than in the radial direction. In the samples (groups 2 and 4) drilled parallel to the bedding, on the contrary, the Young's modulus along the axis is higher than in the radial direction. The observed anisotropy of the rock properties is caused by the direction of maximum stress, which coincides with the direction of sedimentation (perpendicular to the bedding plane). The anisotropy of the properties must be taken into account when conducting laboratory studies and engineering surveys, since it can significantly interfere with understanding the deformation sensitivity of rocks if it is not taken into account or if it is very complex.

The use of non-destructive testing is extremely useful for assessing the stability and influence of atmospheric curing on the properties of replicas over time during storage and in long-term testing programs. Non-destructive testing methods are a useful auxiliary tool to indirectly assess the elastic properties of materials, but not to determine the true stress−strain behavior. A limitation of non-destructive methods is also that the velocity of elastic waves depends on the density and elastic properties of the material, the presence of inhomogeneities and voids, including prefabricated cracks and porosity. Non-destructive techniques are only suitable for intact specimens with ideal shape. Also, when compared with rocks, it was found that 3D LCD printed samples do not show initial anisotropy, which gives them an advantage in the purity of results and reproducibility of experimental studies, as well as the possibility of fine-tuning experimental parameters.

3.2 Assessment with destructive research methods

In geomechanics, destructive methods of measuring the mechanical properties of rocks are often used, which allow estimating the actual mechanical strength and can be used in geoengineering calculations. According to the results of uniaxial compression, it was found that samples with layers at 60° to the load vector showed the highest strength - an average of 158 MPa (with a max of 162 MPa and a min of 156 MPa), while samples with layers at 30° showed the lowest strength, an average of 138 MPa (with a max of 140 MPa and a min of 120 MPa) (Fig. 7). Samples with layers parallel and perpendicular to the load vector have almost the same strength - an average of 146 MPa and 147 MPa, respectively. In addition to strength, the elastic properties of the materials of 3D printed samples are also of interest, a detailed description of which is given below.

3.2.1 Young's modulus

The uniaxial compression tests yielded the stress−strain curves and the total AE signal (see Fig. 7). The stress−strain curve of the samples demonstrates elastic-viscoplastic properties. When loaded to approximately 20 MPa, all samples exhibit a quasi-elastic zone (highlighted in blue in Fig. 7), with stress being linear with strain. All samples exhibit no AE signals exceeding the 40 dB acoustic filter threshold, indicating the absence or low intensity of internal failure. The quasi-elastic deformation zone is of greatest engineering interest, since the parts retain their mechanical properties under elastic stress. In the elastic zone, Young's modulus was determined as a tangent to the stress−strain curve. The tangents to the curves in the elastic zone are described by the equations:

$$\sigma_0 = 4\,272.2\ \varepsilon_a + 0.548\,9 \tag{1}$$

$$\sigma_{30} = 4\,060.8\ \varepsilon_a + 0.458\,8 \tag{2}$$

$$\sigma_{60} = 3\,892.7\ \varepsilon_a + 0.589\,2 \tag{3}$$

$$\sigma_{90} = 4\,006.8\ \varepsilon_a + 0.491\,2 \tag{4}$$

where σ is the stress, ε_a is the axial deformation, the index corresponds to the angle between the printed layers and the load vector.

The coefficients in the equation are the Young's moduli of the specimens. The Young's moduli values range from 3 893 MPa for the specimen with a 60° layer angle to 4 272 MPa for the specimen with layers parallel to the load. The calculated values of the Young's moduli are in good agreement with the non-destructive test results and also show that the specimens have fairly high homogeneity of elastic properties under stresses up to 20 MPa. The analysis showed that the specimens with parallel layers showed the highest values of the Young's modulus, while the specimens with 60° layers showed the lowest. There is a general tendency for the Young's modulus to decrease with increasing layer angle relative to the specimen axis (formulas (1) − (4)). The Young's modulus of the specimens with perpendicular layers is comparable to the Young's modulus of the specimens with 30° layers. The specimens with layers at 0° and 30° to the load vector showed the lowest strength, but showed a high Young's modulus under quasi-elastic loading, indicating high rigidity and low strength. In contrast, the 60° layers specimens have the highest strength but the lowest Young's modulus and, accordingly, lower stiffness under quasi-elastic loading. The discrepancy between the maximum uniaxial compressive stress and Young's modulus suggests different failure mechanisms for specimens with different layer angles.

3.2.2 Poisson's ratio

Based on the axial and radial strains obtained from strain gauges attached to the side surfaces of the samples, Poisson's ratios were calculated under quasi-elastic loading. The values of Poisson's ratios from the layer angle and orientation to the printing axes are shown in Fig. 8. Under quasi-elastic loading, samples with layers parallel to the load vector demonstrate the lowest Poisson's ratio, while samples with 30° layers demonstrate the highest Poisson's ratio.

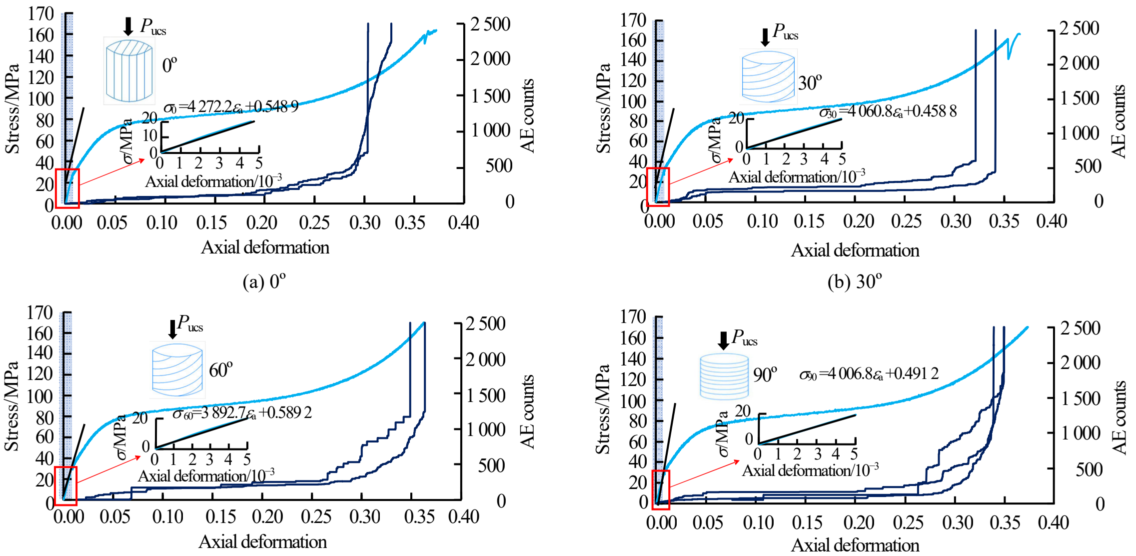

(a) 0°　(b) 30°　(c) 60°　(d) 90°

Note: light blue line – stress, dark blue line – total number of AE signals for the corresponding samples series, and the quasi-elastic deformation zone is highlighted in blue

Fig.7 Stress−strain and total AE signal curves for samples with layers angle

A positive correlation is observed between the increase in the layer angle from 30° to 90° and the decrease in the Poisson's ratio, samples with 0° layers have the lowest Poisson's ratio. The observed correlation is likely due to interlayer slip. Along the *Y*-axis, all samples demonstrate a 40%−60% higher calculated

Poisson's ratio compared to the *X*-axis. The most significant difference in radial deformations along the *X*−*Y* axes (60%) is observed in the samples with layers at 90° to the cylinder axis, indicating high in-plane heterogeneity within the printing layers.

Under uniaxial compression, a complex stress−strain state develops in the sample, characterized by maximum tensile stresses in the center of the sample. In some cases, Poisson's ratios exceed 0.5, indicating a change in the volume of the samples due to internal microcracking. The discrepancy in Poisson's ratios depending on the orientation relative to the printing axes suggests that the expansion of the sample is most likely due to the formation of cracks, predominantly oriented along the *X*-axis of the printer.

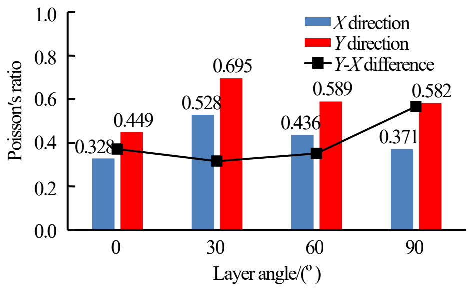

Note: The color corresponds to the print axis along which the deformation is measured (see Fig. 2(d))

Fig.8 Poisson's ratios for samples with different layer orientation

3.2.3 Plastic deformation and acoustic emission

Acoustic emission data are presented in Fig. 7. Comparative analysis showed that for each group of samples the AE curves have the same appearance, which confirms the high convergence and reliability of the experimental results. AE data allowed us to reveal the mechanism of plastic deformation and fracture of samples under high stress[29]. Different modes of sample deformation under loading were established, the stress−strain curve was divided into zones, which are shown in Fig. 9 using the example of a sample with 60° layers. In the initial period of loading, up to approximately 20–30 MPa, a quasi-elastic deformation zone is observed, in which there are no AE signals, and the stress is linear to the deformation. Young's modulus and Poisson's ratio, which were discussed earlier, were calculated in this zone.

Above the quasi-elastic strain limit, plastic deformations begin in the material (elastic-viscoplastic zone), which are accompanied by an increase in the number of AE signals (see Fig.9). Internal microdestruction of the material and the appearance of AE signals begin at approximately the same strain value (~0.025) for all samples (see Fig.7). The duration of this zone varies depending on the orientation of the load vector with respect to the printing layers. The elastic-viscoplastic zone continues up to a stress of about 70 MPa and ends earliest in samples with 30° layers (see Fig.7(b)). Samples with layers parallel to the load vector demonstrate the smallest total number of AE signals in the elastic-viscoplastic zone (see Fig.7(a)). The elastic-viscoplastic zone persists longest in samples with perpendicular layers (see Fig.7(d)). Microcracks that provide further deformation of the sample are initiated in this zone.

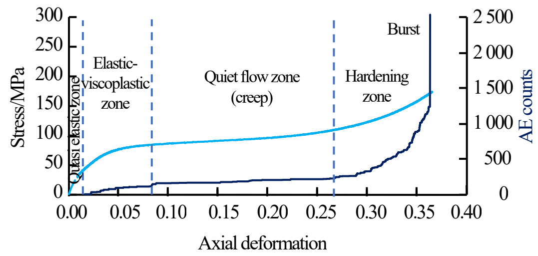

Fig.9 Deformation zones of samples according to acoustic emission data using a sample with 60° layers as an example

When the critical density of microcracks is reached, the material enters a viscous quiet flow regime, characterized by a creep period and a weak increase in the total number of acoustic emission signals[30]. Such deformation is observed in all samples at stresses of approximately 70 to 90 MPa. The greatest deformations occur in the quiet flow zone – from 0.05 to 0.25 with minimal stress growth. The duration of the flow zone in the samples varies significantly depending on the layer angle. Samples with 30° layers demonstrate the longest flow zone. (see Fig.7(b)). Specimens with layers parallel to the load vector exhibit the shortest flow zone (see Fig.7(a)). Samples with 60° and 90° layers show comparable flow zone durations (see Figs.7(c), 7(d)). The quiet flow zone characterizes the ductile properties of the printed material, which is caused by the sliding of the printing layers relative to each other. In samples with a large layer angle (60°), the potential for ductile flow is higher, since more layers pass through the sample axis. These samples have low initial stiffness and a later and smoother ductile to brittle transition, as evidenced by the pattern of changes in the values of the number of AE signals (see Figs.7(c), 7(d)).

At stress above 90 MPa, the flow zone ends in all specimens and the material begins to harden. Hardening is accompanied by a noticeable increase in stress increment and an exponential increase in the number of acoustic emission signals at a constant loading rate. The hardening zone is characterized by internal restructuring and significant compaction of the material. In the hardening zone, the specimens with 60° and 90° layers showed the greatest increase in the number of AE signals – 4 and 7 times more AE signals than in the flow zone, respectively. Specimens with layers parallel to the load vector also showed hardening, as evidenced by the increase in AE signals (see Fig.7(a)). Specimens with 30° layers demonstrated minimal acoustic activity during hardening. After the completion of hardening, a sharp surge in AE signals is observed in all specimens due to failure.

Comparative analysis of AE and uniaxial compression data showed that, despite the similar shape of the stress−strain curves, the failure mechanisms of samples with different layer angles relative to the load vector are different. Due to the different failure mechanisms of samples from the layer angle, when using 3D LCD printed samples in geomechanical studies, these features must be taken into account. It should also be noted that due to the structure of the material, 3D printed material exhibits significant flow properties, which is extremely uncharacteristic of real rocks.

3.2.4 Uniaxial compression of rocks

The results of uniaxial compression tests on rocks are shown in the form of stress−strain curves (see Fig.10).

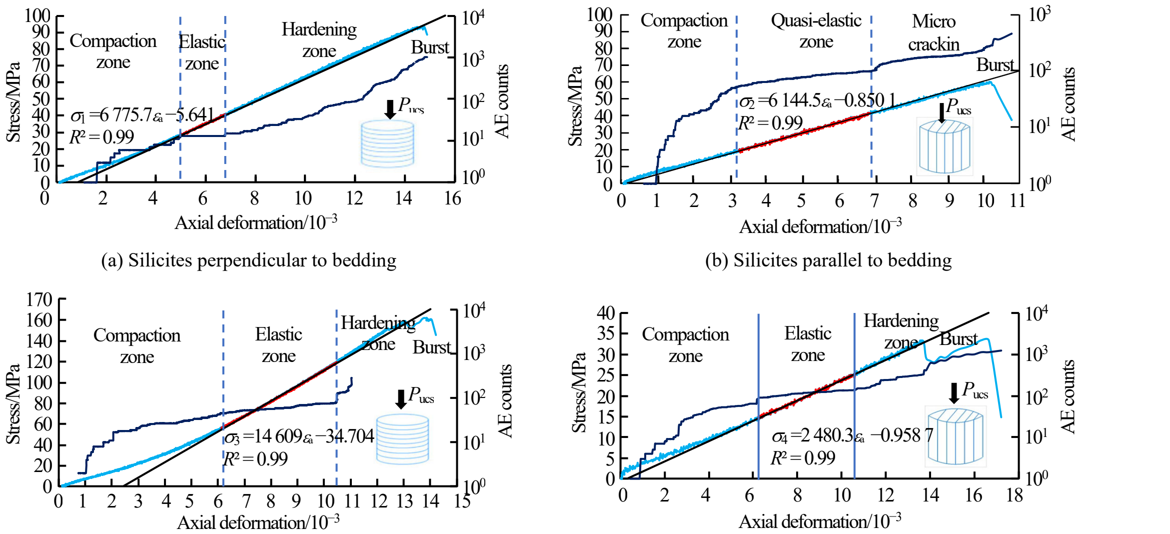

(a) Silicites perpendicular to bedding (b) Silicites parallel to bedding

(c) Silicified dolomites perpendicular to bedding (d) Opoka parallel to bedding

Note: light blue line–stress, dark blue line–total number of AE signals, and red line–elastic deformation zone, tangent to it–for calculating Young's modulus.

Fig.10 Stress−strain and total AE signal curves for rock samples

It was found that in all rock samples in the initial period of uniaxial compression there is a compaction zone, in which the stress nonlinearly increases with deformation (see Fig.10). The compaction zone is caused by the presence of relaxation microcracks in rock samples that arose during excavation. The direction of the microcracks is perpendicular to the main bedding stress and parallel to the bedding, the closure of these cracks under loading occurs without destruction, and therefore, at the very beginning there are no AE signals. When microcracks close, the material hardens, the tangent angle to the stress−strain curve increases. Due to the uneven distribution of stress in the sample, not all microcracks close smoothly during compaction, new microcracks are formed. After a deformation of 0.001, the redistribution of stress in the samples leads to a sharp surge in the intensity of AE signals. The subsequent increase in stress leads to the closure of newly formed microcracks and relaxation cracks, as a result of which the matrix of the samples is almost completely compacted, the elastic zone begins. The zone of elastic deformations in all samples is accompanied by a linear increase in stress from deformation and the absence or weak intensity of AE. The lowest AE intensity is noted in silicite samples with a perpendicular bedding plane (see Fig.10(a)). In silicite samples with bedding planes parallel to the load vector, dolomites and opoka, quasi-elastic deformations occur despite the linearity of the strain-stress curve section, while the AE intensity remains quite high (see Figs.10(b), 10(d)). The tangents to the curves in the elastic zone are described by the equations:

$$\sigma_1 = 6\,775.7\ \varepsilon_a - 5.64 \tag{5}$$

$$\sigma_2 = 6\,144.5\ \varepsilon_a - 0.85 \tag{6}$$

$$\sigma_3 = 14\,609\ \varepsilon_a - 34.70 \tag{7}$$

$$\sigma_4 = 2\,480.3\ \varepsilon_a - 0.95 \tag{8}$$

The index corresponds to the sample group. The coefficients in the equation are the Young's moduli of the specimens.

After elastic deformation, the intensity of internal micro cracking of the samples increases, which is evident from a significant increase in the total number of AE signals. Simultaneously with micro cracking, there is a strengthening of the samples (hardening zone) of silicites perpendicular to the bedding, silicified dolomites and opoka. An increase in the slope of the stress−strain curve is noted (Figs. 10(a), 10(c), 10(d)). In silicite samples drilled parallel to the bedding plane, micro cracking leads to degradation of elastic properties (curve drop) (see Fig.10(b)). Finally, after exceeding the ultimate strength, all samples are destroyed.

The highest uniaxial compressive strength was demonstrated by samples with perpendicular bedding planes–silicites and silicified dolomites– 117 MPa and 186 MPa, respectively. The lowest strength was demonstrated by samples with parallel bedding planes–silicites and opokas–86 MPa and 51 MPa, respectively. Samples with perpendicular bedding planes also demonstrated the highest total deformations (see Figs.10(a), 10(c)), due to the fact that relaxation cracks in them are oriented perpendicular to the load vector.

4 Discussion

4.1 LCD 3D Printing features

The LCD printing process is shown schematically in Fig.11. UV curing of the resin occurs by irradiating a thin layer of resin between the LCD and a previously printed layer mounted on a movable plate. The layer-by-layer manufacturing method determines the laminate structure of the models, which causes anisotropy of the properties of the printed samples from the printing angle. The anisotropy of 3D LCD printed samples is caused by the following features:

(1) Uneven degree of polymerization across the layer thickness (*h*) due to the decrease in UV irradiation intensity with distance from the screen (see Figs.11, 10(b)). As a result of uneven exposure, each layer has a stronger and more brittle structure at the bottom and a weaker, more ductile upper part[31].

(2) Display pixel structure. Transparent pixels of the LCD panel transmit UV light, and opaque pixels determine the shape of the curing layer (see Fig.12). The pixels are separated by partitions, due to which, uneven passage of UV light through the LCD panel leads to a pixelation effect, which is clearly visible on the surface of the printed layer (see Fig.12).

(3) Uneven transmission of UV light along the *X*-*Y* axes of the printer (see Fig.12). Along the *X* axis, the rows of light are solid, and their boundaries have a rounded shape. Along the *Y* axis, there are gaps in the illumination between the rows of pixels, leading to uneven illumination and the appearance of a wavy structure inside the layer.

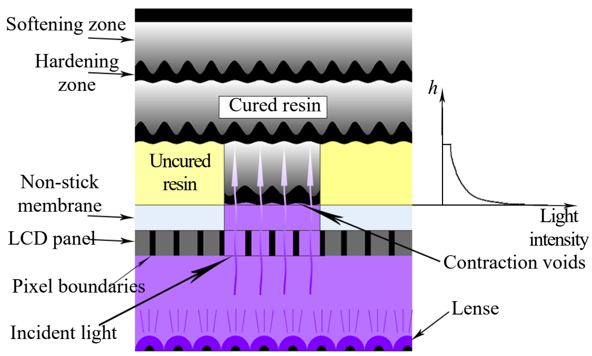

Note: The intensity of UV light changes with distance from the LCD display.

Fig.11 Schematic representation of the UV light curing process of resin in 3D LCD printing

Due to uneven irradiation, a wave-like structure with different degrees of resin polymerization is formed inside the layer (see Fig.11). Using micrographs of chipped samples along the *X* and *Y* printing axes (see Figs.13(a), 13(b)), the internal structure of the layer is reconstructed, which is shown in Fig.13(c). The layer structure is similar to corrugated chips with pronounced waviness along the *Y* axis, the lower part of the layer is a resin with a high degree of polymerization with greater strength and brittleness. The thicker upper part of the layer is a resin with a lower degree of polymerization, lower strength, but greater ductility. The difference in the degree of polymerization is visually evident from the smoothness of the chip surface (see Fig.13(a)). Research by Quagliato et al.[26] found that samples with a low degree of polymerization demonstrate smoother surfaces on chips, while long-term polymerization leads to the appearance of uneven cracks.

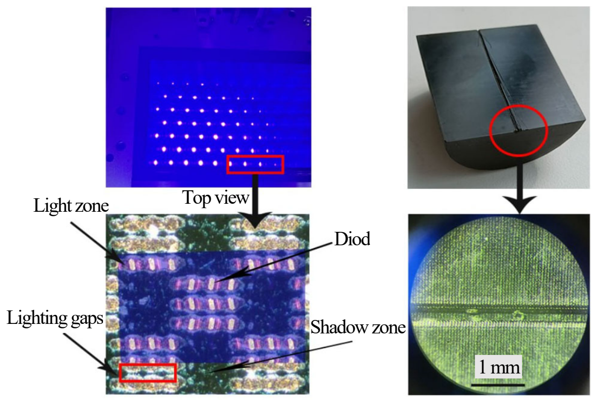

(a) LCD display exposed to UV light and its enlarged image of exposure defects (b) Lower surface of the layer

Fig.12 LCD display exposed to UV light and lower surface of the layer

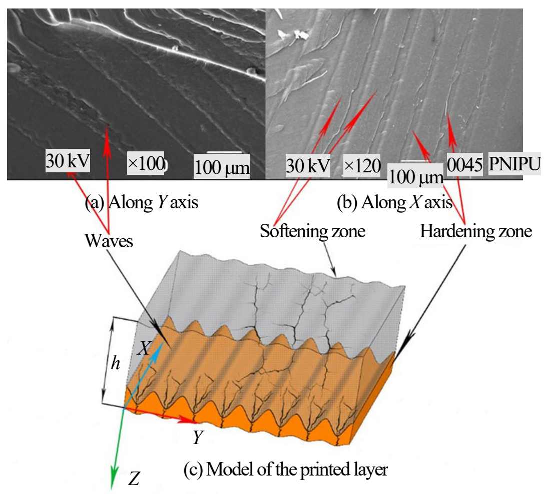

Fig.13 Model of the printed layer and microphotographs of chipped samples along the *Y* and *X* axes

The wavy structure of the resin layer with different degrees of polymerization contributes to its uneven shrinkage and enhances the pixelation effect[32]. It is obvious that the listed features of 3D LCD printing, which determine the layered structure of the printed samples, cause anisotropy of mechanical and elastic properties.

4.2 Effect of 3D LCD printing features, layer angle and orientation on anisotropy

The above-mentioned features of 3D LCD printing do not significantly affect the homogeneity of elastic properties measured using non-destructive testing, as well as under uniaxial compression at a stress of up to 20 MPa. At stress above 20 MPa, anisotropy from the angle and orientation of layers appears. Justification of the dependence of sample properties on the angle and orientation of layers is given below.

In the samples with 0° layers, the load vector coincides with the plane of the printing layer (see Fig.1). Compression is perceived by the strong part of the layers lengthwise, which determines the higher rigidity of the samples and a higher Young's modulus. Due to the longitudinal arrangement of the layers, the material demonstrates the lowest creep tendency among all the tested samples and exhibits more brittle properties. Under loads corresponding to the compaction zone, failure occurs by splitting the layers along the softening part. This failure mode is characterized by a weak, linearly increasing intensity of acoustic emission signals. Visually, the samples demonstrate uniform failure around the circumference, with the formation of longitudinal uniform fragments (see Fig.14(a)). Rupture cracks propagating along the layers are clearly visible at the ends of the destroyed sample and have a preferential direction along the *X* axis (see Fig.14(a)).

In the 30° layer specimens, under uniaxial compression, the shear stresses are parallel to the layer plane. The layer inhomogeneity causes the layers to slide between each other under the shear stress. Throughout the test, the acoustic emission signal intensity is low (see Fig. 7(b)). These specimens also exhibit the lowest compressive strength and the highest Poisson's ratios in both print axes, indicating early and severe microcracking under quasi-elastic loading. The coincidence of the layer angle with the shear stress causes the specimen to crack into large pieces (see Fig.14(b)). The specimen ends show uneven cracking. The diagonal end zones show wear caused by friction against the press plates (see Fig.14(b)). This is typical for the layers in contact with both the upper and lower plates of the load cell. The rest of the ends show less pronounced frictional wear. The specimen ends show different crack patterns (see Fig.14(b)), suggesting that there is no connection between these cracks, as they cannot penetrate the specimen axially due to the blocking effect of the inclined layers.

In the 60° layer specimens, under uniaxial compression, the vertical load acts on the weaker, shear-prone components of the layers. The large layer angle results in a large number of layers along the cylinder axis, causing the slip between the layers to result in the largest longitudinal strain (see Fig.7(c)) and the lowest Young's modulus. Acoustic emission analysis showed that these specimens exhibit the longest compaction period under load, which ultimately contributes to increased material strength. Due to the layer inclination, vertical crack growth is limited; the ends of the 60° layer inclination specimens have fewer cracks compared to the other specimens. In addition, the sliding of the printed layers results in uneven failure of the specimen along the *Y*-axis (see Fig.14(c)).

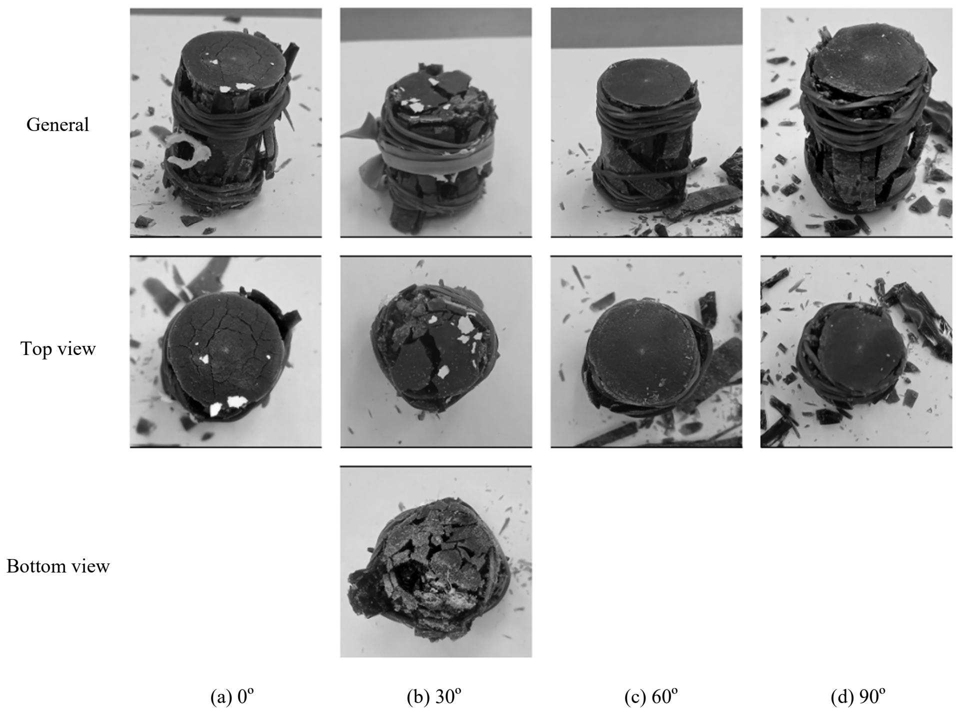

Fig.14 3D printed samples after uniaxial compression test

In the specimens with 90° layers, the vertical load results in compression and transverse extrusion of the softened part of the layers. The hardened part of the layers is weakly compressed, but effectively absorbs the tensile forces arising in the specimen due to compression of the soft part of the layer, preventing its excessive elongation. A distinctive feature of these specimens is the significant anisotropy of the Poisson's ratios observed relative to the printer axes (see Fig.8). This anisotropy is due to the corrugated chip structure of the layers, where the thinned part of the hardened layer acts as stress concentrators (see Fig.13(c)). Under pure tensile loading, the layer rupture occurs predominantly in thin regions along the *Y*-axis (see Figs.13(a), 13(c)). The maximum acoustic emission intensity in the hardening deformation zone among all specimens is caused by rupture of the stronger layers. The perpendicular arrangement of the layers prevents the propagation of vertical cracks at the ends of the destroyed specimens (see Fig.14(d)).

4.3 Comparison of rocks and replicas

The mechanical response of 3D LCD-printed samples differs significantly from the behavior of real rocks under uniaxial compression.

Firstly, the 3D LCD-printed samples do not have the compaction stage in the stress−strain curves, which is typical for rocks in the initial period of loading. However, the 3D LCD-printed samples have a linear stress−strain curve in the initial period of loading and are weakly dependent on the angle of the printing layers, which makes this an advantage in physical modeling, since it allows avoiding states that are not typical for real rocks. Compared to real rocks, despite the different layer angles and orientations, the 3D LCD printed samples are fairly homogeneous, as can be seen using the non-destructive method. Their relative homogeneity is also indicated by the identical shape of the strain-stress curves. In rocks, anisotropy is caused by the bedding conditions of the strata and cannot be ignored when assessing the mechanical behavior under loading. Strong rocks (silicites and silicified dolomites) and weak rocks (opoka) were selected for comparison. Our test results showed that even rocks with a high degree of homogeneity have noticeable anisotropy. Comparative analysis of the strain-stress curves (see Fig.15) showed that the 3D LCD printed samples have Young's moduli smaller than those of dolomites and silicites, but larger than those of opoka. Fig.15 also shows that the elastic deformation zone of the replicas coincides with the elastic deformations of the rocks. Thus, replicas can be analogs of rocks, but only under stresses within the limits of elastic deformations.

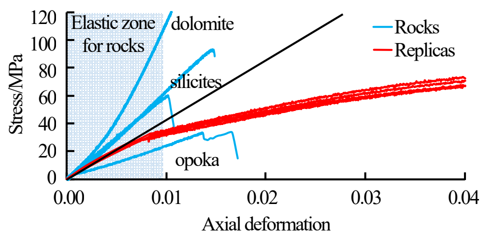

Fig.15 Stress−strain curves for rocks (blue line) and replicas (red line)

Secondly, 3D LCD-printed samples do not exhibit clear peak stress or post-peak behavior, which is characteristic of real rocks. This feature significantly distinguishes replicas from rocks and should be taken into account in physical modeling. At stresses above elastic deformations, microdestruction of 3D LCD printed samples occurs, and due to the peculiarities of the structure of 3D LCD printed materials, a divergence in the stress−strain curves is observed after a stress of 40 MPa. Due to the presence of a weak part of the layer, the replicas are very prone to viscous flow under high loads. Large deformations in replicas compared to rocks are due to the prevalence of cohesive bonds and extremely weak internal friction. Due to the lack of proper friction in replicas, layers slide between each other. The layers slide without much resistance, which is due to the structure of the polymer resin. Despite the sliding of the layers and significant deformation and weak internal friction, the replicas ultimately have significant uniaxial compression strength, comparable to, and in some cases superior to, rocks. The strength of UCS replicas is on average 138 MPa and 162 MPa depending on the angle of the layers, for rocks and 51 MPa to 186 MPa. However, before destruction, significant deformations accumulate in the replicas - up to 0.37, the replicas take a barrel-shaped form before destruction (see Fig.16(b)). The deformation in rocks is barely noticeable (see Fig.16(d), 16(e)) even after destruction and does not exceed 0.015.

The micrographs (see Fig.17) show that the 3D printed sample has a smooth chip surface, nothing prevents the layers from sliding and microcracks from growing. The fine-grained structure in rocks has high cohesion, as well as significant friction, the crack is uneven, torn (see Fig.17(b)), the granular structure prevents smooth sliding of microcracks.

The destroyed rock samples have no visible features from the bedding angle, unlike the replicas. The silicite samples, perpendicular and parallel to the bedding, have almost the same type of destruction with large fragmentation and longitudinal main cracks extending to the ends of the samples (see Fig.18(a)). The dolomite and opokas samples, although they have different strength and bedding angle (see Fig.18(b)), but equally exhibit high brittleness, which is expressed in significant fragmentation of the samples. In the dolomites and opokas, there are many cracks at the ends, this indicates the predominance of the brittle destruction mechanism over the ductile one. In the replicas with 0° layers, there are also many cracks at the ends, but unlike the rocks, these cracks are formed as a result of delamination and are characteristic only of these samples. In the replicas with 60° and 90° layers, in which long-term strengthening zones were observed, there are no longitudinal brittle cracks on the ends, which also confirms that the material of the replicas is more ductile than brittle.

Thus, as a result of the studies of the mechanical properties of rock replicas, it was established that the 3D LCD printing method is suitable for studying the properties of rock-like samples under minor loads that do not lead to internal destruction. Samples printed using the 3D LCD method are not complete analogues of rocks and cannot completely replace the study of real rocks especially in studies involving destruction. In order to use the 3D LCD printing method to create replicas of rocks for destructive testing, it is first necessary to solve the issue of internal friction of the material, which is absent. However, using this method to create rock replicas to study processes in rocks under purely elastic loading will allow us to evaluate the mechanical behavior of rocks with various features that can be adjusted in a wide range. An example of using 3D LCD printing in geomechanics to study the transport properties of rocks under cyclic loading is shown further.

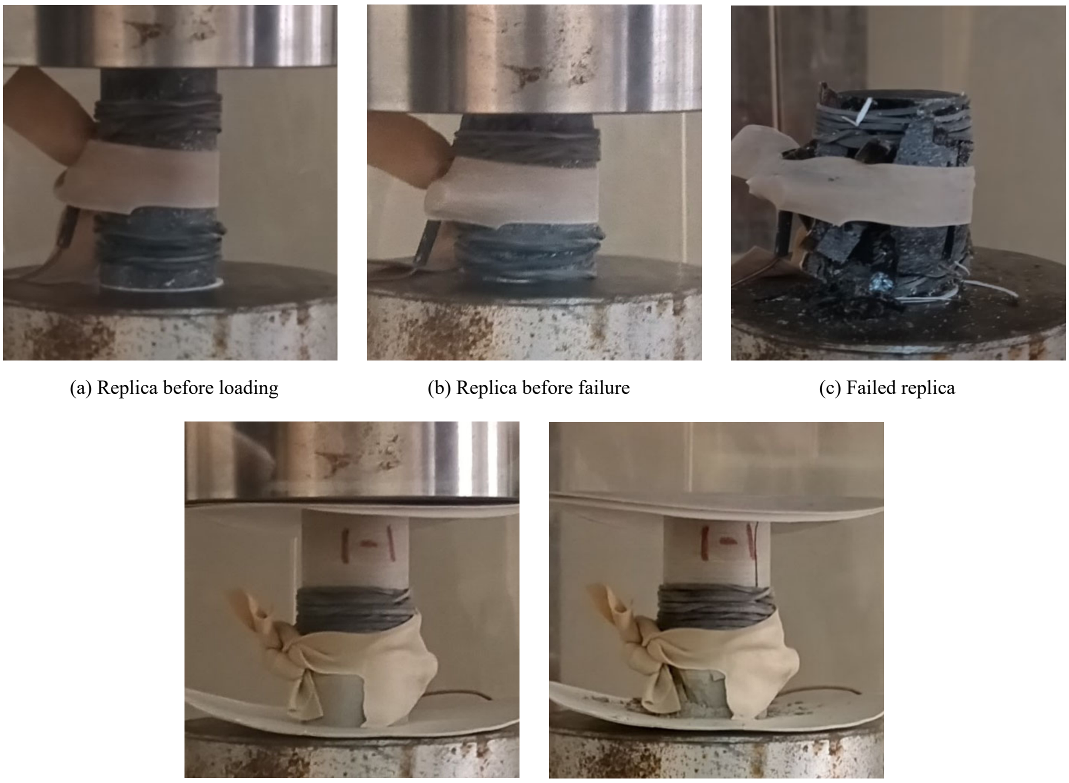

(a) Replica before loading (b) Replica before failure (c) Failed replica

(d) Rock before loading (e) Failed rock

Fig.16 Photos of specimens under loading

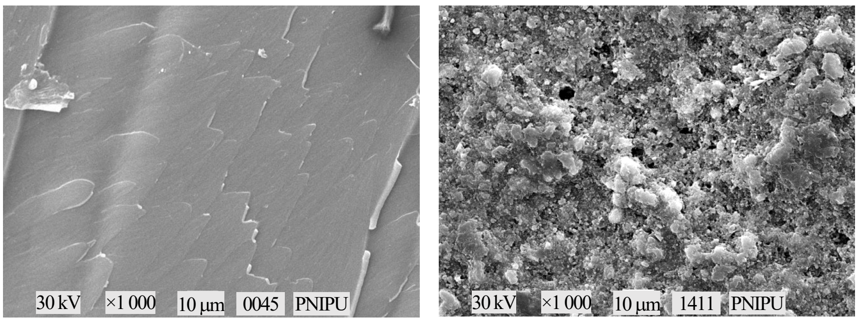

(a) 3D printed sample (b) Silicite

Fig.17 Microphotograph of the chip surface

4.4 Example of using 3D LCD printed samples in flooding with cyclic loading

The study of flow in porous media is traditionally carried out on bulk models consisting of sand or glass beads, as well as on rock samples. The advantage of using bulk models is the ability to control the effect of grain size on transport properties. However, under cyclic loading, the use of bulk models is of little use due to the collapse of grains. The advantage of using rocks is the real flow conditions in natural environments with reference to specific rocks. However, the results of experiments with real rocks can be affected by extraneous factors, such as changes in the physicochemical state during reactive flow, blocking of pores due to detachment and migration of colloids, plastic deformations due to microdestruction. Therefore, the description of the exact law of permeability change under cyclic loading of rocks is difficult. To minimize the influence of all the above factors on the reliability of experimental studies under cyclic loading, we proposed to use 3D LCD printed replicas of core plugs as samples. The methodology involved flooding tests with cyclic loading of 3D printed replicas with grooves of varying sizes in the middle of the sample. Model creation, printing process, and finished replicas are shown in Fig. 19. P_{conf} is confining pressure. First, a digital 3D model of a half of the sample with a groove in the middle (see Fig.19(a)) and the second adjacent half without a groove (blank) was created. In order to minimize scattering effects during printing, the groove has a rectangular shape (see Fig.19(b)). Samples were printed on supports with the groove facing the display (see Fig.19(c)).

(a) Samples perpendicular to bedding (b) Samples parallel to bedding

Fig.18 Rock samples after uniaxial compression test

After printing, the replicas were visually inspected for surface smoothness (see Fig.19(d)) and the cleanliness of the groove (see Fig.19(e)). Next, the assembled model (see Fig.19(f)) was placed in the core holder of the UltraPoroPerm-500 setup (see Fig.19(g)). Flooding was carried out with a constant nitrogen flow rate under cyclic confining pressure. More details on the research methodology can be found in literature [33]. Since the replica is not porous, and nitrogen flows through the channel, conductivity was measured instead of permeability. Instantaneous conductivity C of the samples for nitrogen was determined as the ratio of nitrogen flow rate taking into account compressibility to the pressure gradient in the sample using the formula:

$$C = Q / \left[\left(P_{\text{in}}^2 - P_{\text{o}}^2 \right) / \left(P_{\text{o}} L \right) \right] \quad (9)$$

where Q is nitrogen flow rate (cm^3/s); P_{in} is nitrogen injection pressure (Pa); P_{o} is pressure at the outlet of the sample(Pa); and L is the length of the sample (mm).

To conduct comparative filtration tests, samples of intact porous sandstone and impermeable silicified dolomite, artificially split in half, were selected. (see Fig. 20).

Comparative results of conductivity tests of a replica with width (w) 350 μm and depth (h) 150 μm groove (hereinafter referred to as 350-150) and rock samples are shown in the graphs (see Figs.21−23). Upon visual comparison, the conductivity dynamics of the replica are identical to those of a real porous and artificially split sample. Upon closer examination (see Figs.21(b), 22(b), 23(b)), it can be seen that with increasing confining pressure, the replica and rocks conductivity decreases in the same pattern, first a sharp decrease, and then a smooth creeping decrease in conductivity. A smoother conductivity dynamics line is in samples with an artificial crack, but the same sample has the largest conductivity amplitude under cyclic loading (see Figs.22(b), 22(c)). Porous samples have a greater scatter in conductivity dynamics, this is due to a large number of pores and microcracks, changing geometry during creep. Replicas combine a fairly high smoothness of conductivity dynamics inherent in artificial cracks and a scatter in conductivity dynamics as in porous samples.

The instantaneous decrease in conductivity occurs due to a sharp increase in confining pressure, and creep is caused by sliding of the two halves relative to each other in the replica and in a sample with an artificial crack and sliding of microcracks in the porous sandstone sample. Such behavior confirms the presence of relaxation microcracks in the sandstone caused by its excavation from a depth of 1 800 m during drilling of an oil well.

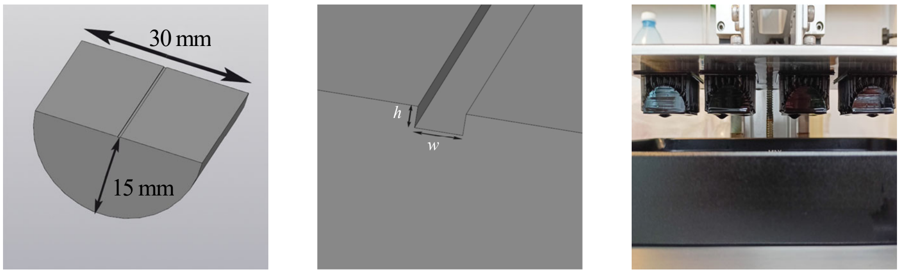

(a) Shape and size of the model half (b) Shape of the groove (c) Printing of the model

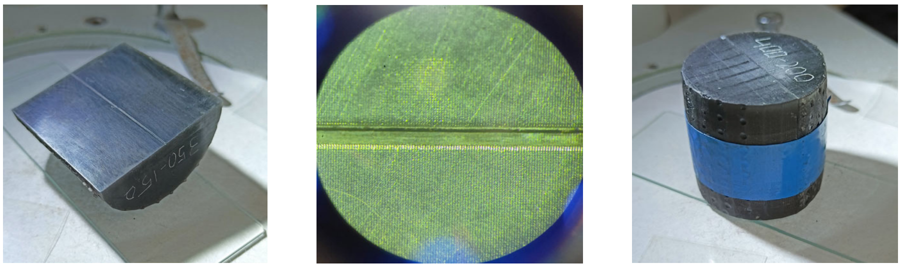

(d) Printed half of the sample with a groove (e) View of the groove under a microscope (f) A core plug model assembled from two halves

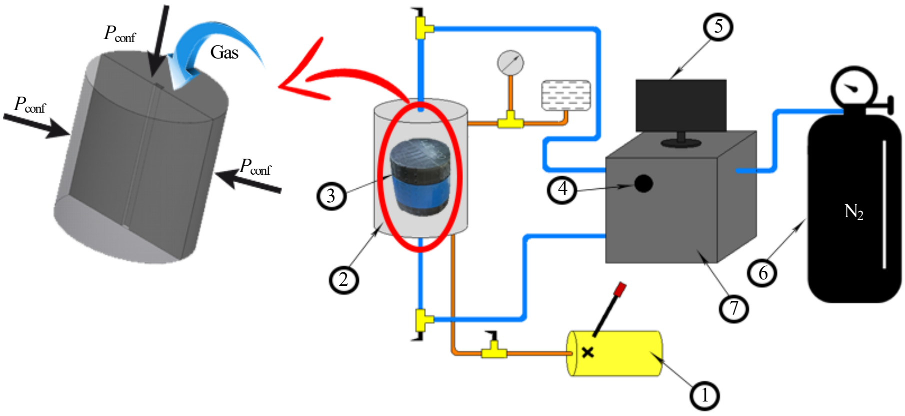

(g) Scheme of the flooding setup

Note: 1 – hand pump for confining pressure, 2 – core holder, 3 – core plug model, 4 – nitrogen flow regulator, 5 – PC, 6 – nitrogen cylinder, 7 – measuring system.

Fig.19 Methodology for manufacturing and testing a core plug model with a groove in the middle

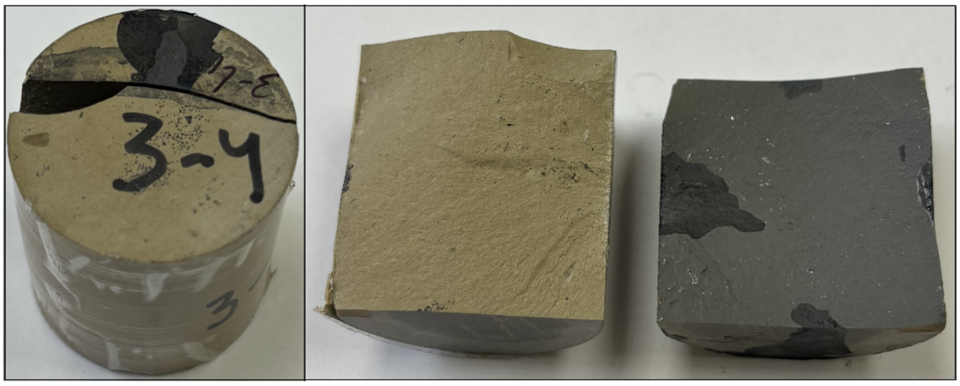

Fig.20 Assembled specimen with artificial crack

When the confining pressure decreases (see Figs.21(c), 22(c), 23(c)), the conductivity is restored in samples first instantly, and then in a creeping mode due to the accumulated internal energy. The same in the replica and in the porous sandstone sample, under loading, the conductivity curve has a smooth appearance, without significant jumps, whereas under unloading, the conductivity curve has a jagged appearance. In the artificially split sample, the conductivity recovery curve is smooth (see Fig.23(c)). The difference is that in the porous sandstone and the replica, the conductivity recovery is due to the stick-slip sliding of the surfaces of the halves and microcracks during shape restoration[34-35].

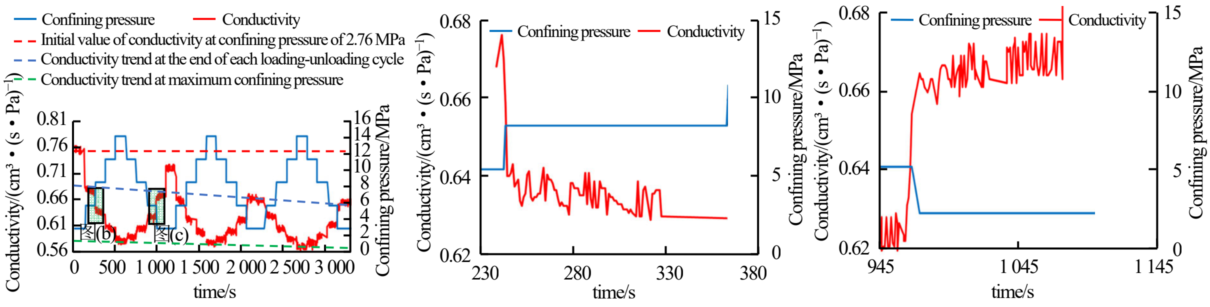

(a) Full log (b) Fragment with loading step (c) Fragment with unloading step

Fig.21 Conductivity dynamic of the intact porous sandstone sample during cyclic loading

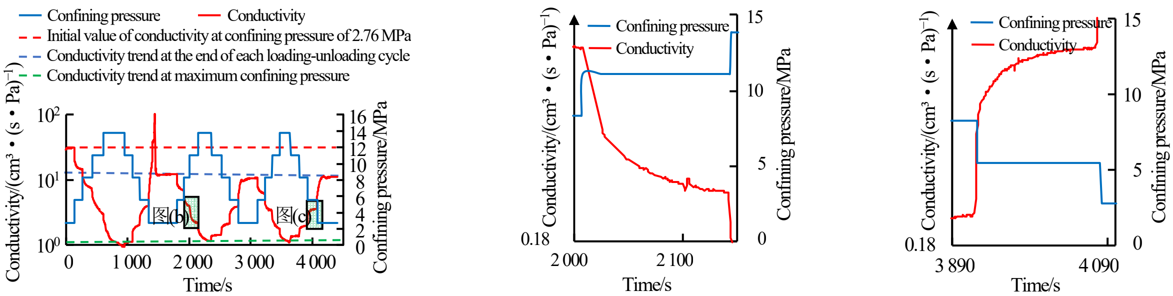

(a) Full log (b) Fragment with loading step (c) Fragment with unloading step

Fig.22 Conductivity dynamic of the nonpermeable artificially fractured sample during cyclic loading

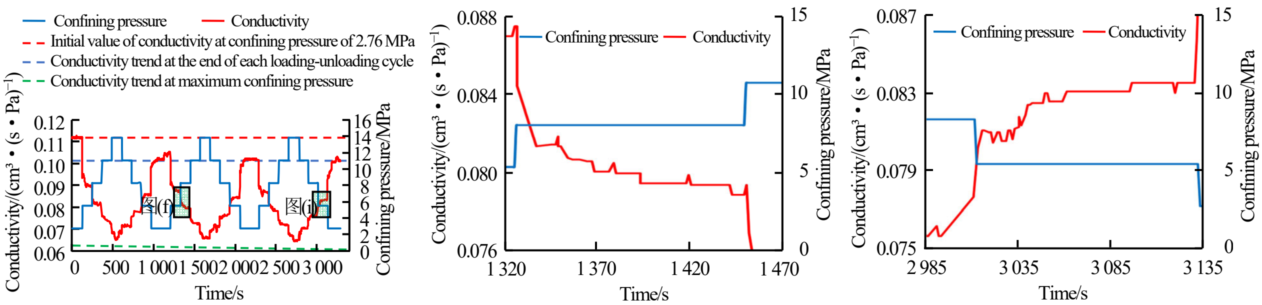

(a) Full log (b) Fragment with loading step (c) Fragment with unloading step

Fig.23 Conductivity dynamic of the printed sample (350-150) during cyclic loading

The comparative analysis also showed that in the replica, unlike the rock samples, the deformation does not accumulate under cyclic loading. In the replica, after unloading in the first cycle and in subsequent cycles, the conductivity at the maximum and minimum confining pressures remains at the same values (the blue and green dotted lines in Fig.22(a) show the conductivity trend). In the sandstone sample, compaction is observed under cyclic loading, which is expressed in a gradual decrease in conductivity from cycle to cycle (the inclined blue and green dotted lines in Fig.21(a) show a trend toward a decrease in conductivity). In the artificial split sample Fig.22(a), the decrease in conductivity occurs as in the replica Fig.23(a).

The conductivity of the replicas and the rock samples are equally well described (R^2=0.99) by classical power equations from the confining pressure (Fig.24)[36-37]. It was also found that the replicas have a smaller permeability hysteresis under loading in each cycle. For the replicas, the confining pressure-conductivity curves are almost parallel under loading and unloading. The exponents of the power equations describing the change in conductivity of replicas under loading and unloading differ insignificantly and are −0.282 and −0.266, respectively (see Fig.24(c)). In the sample with an artificial crack, a significant decrease in conductivity is observed during the first loading, but in the following cycles the conductivity curves during loading and unloading are parallel. The exponents of the power equations describing the change in conductivity of artificial cracked sample under loading and unloading differ insignificantly and are −1.3 and −1.31, respectively (see Fig.24(b)). In the sandstone samples, the permeability hysteresis is clearly expressed, the exponents of the power equations under loading and unloading are −0.133 and −0.085, respectively.

An analysis of the influence of the groove area on their conductivity was also performed, the results are shown in Fig.25. The area-conductivity curve has the classical form of the dependence of permeability on porosity and is very well described by a power equation (R^2=0.97).

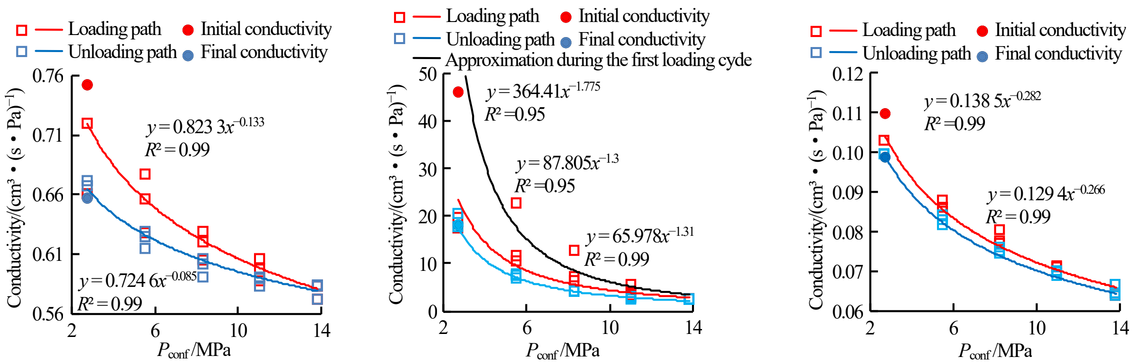

(a) Intact porous sandstone sample (b) Nonpermeable artificially fractured sample (c) Printed sample

Fig.24 Conductivity of samples as a function of confining pressure

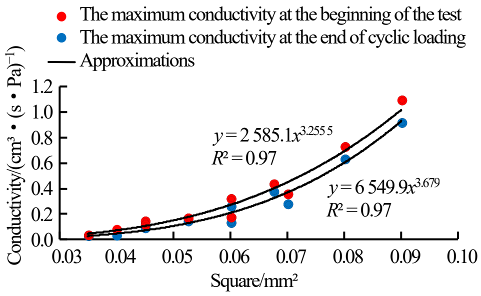

Fig.25 The dependence of the replica conductivity on the initial groove area

Thus, based on the comparative analysis, it has been established that the use of 3D LCD printing technology can be used in geosciences, and in particular in studies of the effect of cyclic deformations on the conductivity of thin capillaries, which can serve as analogs of porous medium channels. The use of printed replicas in the study of flow modes allows avoiding the influence of extraneous factors, such as permeability hysteresis, migration of colloids, etc. Also, with the help of 3D LCD printing, it is possible to create channels with different configurations, which will allow more accurately establishing flow laws in porous and fractured media.

5 Conclusion

The aim of this study was to experimentally evaluate the possibility of using the 3D LCD printing method to create replicas of rocks suitable for geomechanical studies. As a result of the experimental studies, it was established: UV curing for 4 minutes stabilizes 3D-printed rock replicas (29 mm diameter), with properties remaining stable for at least 14 days under dark storage.

The replicas exhibit uniform elastic properties and homogeneity, with consistent wave velocities across layers and Young’s moduli ranging from 3 893 MPa (60° layers) to 4 272 MPa (parallel layers) under ≤20 MPa stress.

Layer orientation affects mechanical behavior: 60° layers showed the highest compressive strength (158 MPa), while 30° layers were weakest (138 MPa). Failure mechanisms vary by angle, necessitating consideration in geomechanical applications.

While suitable for elastic-loading studies (e.g., cyclic deformation effects on porous media), printed replicas cannot fully replace real rocks in destructive tests due to lacking internal friction and distinct failure behaviors.

Declaration of competing interest

The authors declare that they have no known competing financial interests or personal relationships that could have appeared to influence the work reported in this paper.

References

[1] DONG D, SU H J, LI X, et al. Microstructures and mechanical properties of biphasic calcium phosphate bioceramics fabricated by SLA 3D printing[J]. Journal of Manufacturing Processes, 2022, 18: 433-443.

[2] PATIÑO J E, MIELE F, PEREZ A J, et al. Replication of soil analogues at the original scale by 3D printing: Quantitative assessment of accuracy and repeatability of the pore structural heterogeneity[J]. Advances in Water Resources, 2024, 192: 104795.

[3] TURBAKOV M, GUZEV M, RIABOKON E, et al. 3D printing for core flooding tests evaluating[C]// the 2023 International Field Exploration and Development Conference. Wuhan: Springer, 2024.

[4] KERR T. FDM 3D printing[M]//3D Printing. [S. l.]: Springer Cham, 2022.

[5] MORETTINI G, PALMIERI M, CAPPONI L, et al. Comprehensive characterization of mechanical and physical properties of PLA structures printed by FFF-3D-printing process in different directions[J]. Progress in Additive Manufacturing, 2022, 7: 1111-1122.

[6] ALMETWALLY A G, JABBARI H. 3D-printing replication of porous media for lab-scale characterization research[J]. ACS Omega, 2021, 6(4): 2655-2664.

[7] VIDHU N, GUPTA A, SALAJEGHE R, et al. A computational model for stereolithography apparatus (SLA) 3D printing[J]. Progress in Additive

Manufacturing, 2024, 9: 1605-1619.
[8] ISHUTOV S. Establishing framework for 3D printing porous rock models in curable resins[J]. Transp Porous Media, 2019, 129: 431-448.
[9] YU Z D, LI X Q, ZUO T X, et al. High-accuracy DLP 3D printing of closed microfluidic channels based on a mask option strategy[J]. The International Journal of Advanced Manufacturing Technology, 2023, 127: 4001-4012.
[10] SAITTA L, TOSTO C, PERGOLIZZI E, et al. Liquid crystal display (LCD) printing: a novel system for polymer hybrids printing[J]. Macromolecular Symposia, 2021, 395. DOI:org/10.1002/masy.202000254.
[11] CHEN S, ZHANG J, YIN D, et al. Visualizing experimental investigation on gas–liquid replacements in a microcleat model using the reconstruction method[J]. Deep Underground Science and Engineering, 2023, 2(3): 295-303.
[12] ALMUBARAK M, GERMAINE J T, EINSTEIN H H. Fracturing processes in specimens with internal vs. throughgoing flaws: an experimental study using 3d printed materials[J]. Rock Mechanics and Rock Engineering, 2024. DOI.org/10.1007/s00603-024-04168-y.
[13] IBRAHIM E R, JOUINI M S, BOUCHAALA F, et al. Simulation and validation of porosity and permeability of synthetic and real rock models using three-dimensional printing and digital rock physics[J]. ACS Omega, 2021, 6(47): 31775-31781.
[14] WU H, JU Y, HAN X, et al. Size effects in the uniaxial compressive properties of 3D printed models of rocks: an experimental investigation[J]. International Journal of Coal Science & Technology, 2022,9: 83.
[15] LI Y, TENG Z. Effect of printing orientation on mechanical properties of SLA 3D - printed photopolymer[J]. Fatigue & Fracture of Engineering Material of Structure. 2024, 47(5): 1531-1545.
[16] MONZÓN M, ORTEGA Z, HERNÁNDEZ A, et al. Anisotropy of photopolymer parts made by digital light processing[J]. Materials, 2017, 10(1): 64.
[17] SAINI J, DOWLING L, KENNEDY J, et al. Investigations of the mechanical properties on different print orientations in SLA 3D printed resin[J]. Journal of Mechanical Engineering Science, 2020, 234(11): 2279-2293.
[18] FARKAS A Z, GALATANU S V, NAGIB R, The influence of printing layer thickness and orientation on the mechanical properties of DLP 3D-printed dental resin[J]. Polymers, 2023, 15(5): 1113.
[19] KEBLER A, HICKEL R, ILIE N, In vitro investigation of the influence of printing direction on the flexural strength, flexural modulus and fractographic analysis of 3D-printed temporary materials[J]. Dental Material Journal, 2021,40(3): 641-649.
[20] PUEBLA K, ARCAUTE K, QUINTANA R, et al. Effects of environmental conditions, aging, and build orientations on the mechanical properties of ASTM type I specimens manufactured via stereolithography[J]. Rapid Prototyping Journal, 2012, 18(5): 374-388.
[21] DULIEU BARTON J M, FULTON M C. Mechanical properties of a typical stereolithography resin[J]. Strain, 2000, 36(2): 81-87.
[22] SHIRINBAYAN M, ZIRAK N, SADDAOUI O, et al. Effect of build orientation and post-curing of (meth)acrylate - based photocurable resin fabricated by stereolithography on the mechanical behavior from quasi-static to high strain rate loadings[J]. The International Journal of Advanced Manufacturing Technology, 2022, 123: 1877-1887.
[23] COSMI F, MASO A D. A mechanical characterization of SLA 3D-printed specimens for low-budget applications[J]. Materialstoday: Proceedings, 2020, 32(2): 194-201.
[24] PANDZIC A. Influence of layer height, build orientation and post curing on tensile mechanical properties of SLA 3D printed material[C]//32nd Daaam International Symposium on International Symposium on Intelligent Manufacturing and Automation. Vienna: [s. n.], 2021.
[25] ASTM International. Standard test methods for compressive strength and elastic moduli of intact rock core specimens under varying states of stress and temperatures[S]. West Conshohocken, PA: ASTM, 2023.
[26] QUAGLIATO L, KIM S Y, RYU S C. Quasi-ductile to brittle transitional behavior and material properties gradient for additively manufactured SLA acrylate[J]. Materials Letters, 2022, 329: 133121.
[27] SHIRINBAYAN M, ZIRAK N, SADDAOUI O, et al. Effect of build orientation and post-curing of (meth)acrylate - based photocurable resin fabricated by stereolithography on the mechanical behavior from quasi-static to high strain rate loadings[J]. The International Journal of Advanced Manufacturing Technology, 2022, 123: 1877-1887.
[28] FARKAS A Z, GALATANU S V, NAGIB R. The influence of printing layer thickness and orientation on the mechanical properties of DLP 3D-printed dental resin[J]. Polymers, 2023, 15(5): 1113.
[29] JIANG Y, LIANG B, WANG D, et al. Experimental study on the damage characteristics of cyclic disturbance and acoustic emission characteristics of different types of sandstones under high stress in deep

mines[J]. Deep Underground Science and Engineering, 2025, 4(2): 278-289.

[30] LI X, LI L, YAN F, et al. An analytical solution of direction evolution of crack growth during progressive failure in brittle rocks[J]. Deep Underground Science and Engineering, 2025, 4(3): 452-460.

[31] LEE E D, SIM J H, KWEON H J, et al. Determination of process parameters in stereolithography using neural network[J]. KSME International Journal, 2004, 18: 443-452.

[32] MEHDIKHANI M, GORBATIKH L, VERPOEST I, et al. Voids in fiber-reinforced polymer composites: a review on their formation, characteristics, and effects on mechanical performance[J]. Journal of Composite Materials, 2018, 53(12): 1579-1669.

[33] KOZHEVNIKOV E V, TURBAKOV M S, RIABOKON E P, et al. Cyclic confining pressure and rock permeability: mechanical compaction or fines migration[J]. Heliyon, 2023, 9(11): e21600.

[34] RIABOKON E, GLADKIKH E, TURBAKOV M, et al. Effects of ultrasonic oscillations on permeability of rocks during the paraffinic oil flow[J]. Géotechnique Letters, 2023, 13(3): 151-157.

[35] KAREV V I, KHIMULIA V V, SHEVTSOV N I. Experimental studies of the deformation, destruction and filtration in rocks: a review[J]. Mechanics of Solids, 2021, 56: 613-630.

[36] KOZHEVNIKOV E V, TURBAKOV M S, RIABOKON E P, et al. Apparent permeability evolution due to colloid migration under cyclic confining pressure: on the example of porous limestone[J]. Transport in Porous Media, 2023, 151: 263-286.

[37] KHIMULIA V, KAREV V, KOVALENKO Y, et al. Changes in filtration and capacitance properties of highly porous reservoir in underground gas storage: CT-based and geomechanical modeling[J]. Journal of Rock Mechanics and Geotechnical Engineering, 2024, 16(8): 2982-2995.